

A Simple Approach for Disentangling Vortical and Wavy Motions of Oceanic Flows

CHUANYIN WANG,^a ZHIYU LIU ^a AND HONGYANG LIN^a

^a *State Key Laboratory of Marine Environmental Science, and Department of Physical Oceanography, College of Ocean and Earth Sciences, Xiamen University, Xiamen, China*

(Manuscript received 12 July 2022, in final form 31 January 2023, accepted 12 February 2023)

ABSTRACT: A long-standing challenge in dynamical oceanography is to distinguish nonlinearly intermingled dynamical regimes of oceanic flows. Conventional approaches focus on time-scale or space-scale decomposition. Here, we pursue a dynamics-based decomposition, where a mean flow is introduced to extend the classic theory of wavy and vortical modes. Mainly based on relative magnitudes of the relative vorticity and the modified horizontal divergence in spectral space, the full flow is decomposed into wavy and vortical motions. The proposed approach proves simple and efficient and can be used particularly for online disentangling vortical and wavy motions of the simulated flows by ever-popular tide-resolving high-resolution numerical models. This dynamical approach, combined with conventional time-scale- or space-scale-based approaches, paves the way for online mixing parameterizations using model simulated vortical (for isopycnal mixing) and wavy (for diapycnal mixing) motions and for understanding of multiregime and multiscale interactions of oceanic flows.

KEYWORDS: Internal waves; Mesoscale processes; Ocean dynamics; Shallow-water equations

1. Introduction

Vortical and wavy motions are prototypes of oceanic flows. Typical examples of vortical and wavy motions are mesoscale flows and internal gravity waves (IGWs), respectively. The most recent research estimated that mesoscale flows contribute more than 50% of surface geostrophic kinetic energy (Storer et al. 2022). Mesoscale flows stir active and passive tracers to induce isopycnal mixing, which needs to be parameterized in non-eddy-resolving ocean general circulation models (OGCMs; Gent and McWilliams 1990; Griffies 1998). Energetically, mesoscale flows tend to transfer the kinetic energy to large scales (e.g., Scott and Wang 2005). By contrast, the energy of IGWs is generally transferred toward small scales and small-scale IGWs in turn are prone to breaking to produce diapycnal mixing (e.g., McComas and Müller 1981; Polzin and Lvov 2011) that is unresolved by present (and foreseeable future) OGCMs; information of large-scale IGW fields is thus essential for the faithful parameterization of diapycnal mixing (e.g., St. Laurent et al. 2002; Jayne 2009).

Due to the dynamical disparities and associated ramifications, it is of practical and theoretical interest to distinguish between vortical and wavy motions. Toward this end, four general approaches, which leverages differences in space and/or time scales of these two prototypical motions, are widely used in oceanographic studies: (i) the temporal filtering which

decomposes the full flow into wavy and vortical motions using cut-off frequencies (e.g., Barkan et al. 2017, 2021; Naveira Garabato et al. 2022), (ii) the spatial filtering which separates the full flow into wavy and vortical components using a cutoff wavelength (Sugimoto and Plougonven 2016; Torres et al. 2019), (iii) the spatiotemporal filtering which realizes spectral decompositions through a combination of spatial and temporal filterings (Qiu et al. 2018; Torres et al. 2018), and (iv) Lagrangian filtering which separates wavy motions from nonwavy motions through temporal filtering in a Lagrangian frame of reference (Nagai et al. 2015; Shakespeare and Hogg 2017, 2019; Bachman et al. 2020; Shakespeare et al. 2021). For example, Barkan et al. (2021) temporally coarse-grained the full flow to emphasize the catalytic role played by IGWs in forward cascading the mesoscale kinetic energy. Based on the slope discontinuity of sea surface height wavenumber spectra during summertime, Torres et al. (2019) spatially filtered the full flow to get vortical and wavy motions and quantified the kinetic energy transfers between them. Using the locally lowest tidal frequency and the dispersion relation of mode-10 IGWs, Qiu et al. (2018) spatiotemporally filtered the full flow to explore the seasonality of the transition length scale from vortical to wavy motions in the global ocean. In contrast to abovementioned methods which are applied in the Eulerian frame of reference, Shakespeare et al. (2021) temporally high-pass filtered the full flow in a frame of reference moving with the full flow to extract wavy motions (the rest is taken as non-wavy motions). Obviously, the temporal filtering, the spatial filtering, and the spatiotemporal filtering are based on assumed time-scale or space-scale separations, and thus often give decompositions with overlapping contributions from the vortical and wavy motions; Lagrangian filtering requires particle tracking and is thus computationally expensive. This motivates us to develop a simple approach for disentangling vortical and wavy motions of oceanic flows based on their contrasting dynamical characteristics.

 Denotes content that is immediately available upon publication as open access.

 Supplemental information related to this paper is available at the Journals Online website: <https://doi.org/10.1175/JPO-D-22-0148.s1>.

Corresponding author: Zhiyu Liu, zyliau@xmu.edu.cn

DOI: 10.1175/JPO-D-22-0148.1

© 2023 American Meteorological Society. For information regarding reuse of this content and general copyright information, consult the [AMS Copyright Policy \(www.ametsoc.org/PUBSReuseLicenses\)](#).

The remainder of this paper is structured as follows: [section 2](#) details the proposed methodology of the dynamical decomposition of vortical and wavy motions. [Section 3](#) describes a proof-of-concept application of the proposed methodology to simulated flows in the central South China Sea. Discussion and a summary are presented in [section 4](#).

2. Methodology

The primitive equations of oceanic flows in the Cartesian system read (e.g., [Vallis 2006](#))

$$\begin{cases} \frac{\partial u}{\partial t} + U \frac{\partial u}{\partial x} + V \frac{\partial u}{\partial y} + \frac{\partial w}{\partial z} - f_0 v = -\frac{1}{\rho_0} \frac{\partial p}{\partial x} + S^u \\ \frac{\partial v}{\partial t} + U \frac{\partial v}{\partial x} + V \frac{\partial v}{\partial y} + \frac{\partial w}{\partial z} + f_0 u = -\frac{1}{\rho_0} \frac{\partial p}{\partial y} + S^v \\ \frac{\partial p}{\partial z} = -\rho g \\ \frac{\partial u}{\partial x} + \frac{\partial v}{\partial y} + \frac{\partial w}{\partial z} = 0 \\ \frac{\partial \rho}{\partial t} + U \frac{\partial \rho}{\partial x} + V \frac{\partial \rho}{\partial y} + \frac{\partial w}{\partial z} - w \frac{N^2 \rho_0}{g} = S^\rho \end{cases}, \quad (1)$$

where (u, v, w) denote the velocity, f_0 the Coriolis parameter on the f plane, ρ_0 the reference density, ρ the density perturbation, p the pressure perturbation, g the acceleration due to gravity, and N the background buoyancy frequency. The terms S^u , S^v , and S^ρ are subgrid parameterizations and/or sources/sinks that are represented symbolically. To seek analytical solutions, we ignore S^u , S^v , and S^ρ and assume that the background flow $(U, V, 0)$ is horizontally uniform and temporally constant. The equation set (1) can thus be linearized as follows

$$\begin{cases} \frac{\partial u}{\partial t} + U \frac{\partial u}{\partial x} + V \frac{\partial u}{\partial y} - f_0 v = -\frac{1}{\rho_0} \frac{\partial p}{\partial x} \\ \frac{\partial v}{\partial t} + U \frac{\partial v}{\partial x} + V \frac{\partial v}{\partial y} + f_0 u = -\frac{1}{\rho_0} \frac{\partial p}{\partial y} \\ \frac{\partial p}{\partial z} = -\rho g \\ \frac{\partial u}{\partial x} + \frac{\partial v}{\partial y} + \frac{\partial w}{\partial z} = 0 \\ \frac{\partial \rho}{\partial t} + U \frac{\partial \rho}{\partial x} + V \frac{\partial \rho}{\partial y} - w \frac{N^2 \rho_0}{g} = 0 \end{cases}. \quad (2)$$

Based on separation of variables

$$\begin{cases} u(x, y, z, t) = u_h(x, y, t)F(z) \\ v(x, y, z, t) = v_h(x, y, t)F(z) \\ p(x, y, z, t) = \rho_0 g \eta(x, y, t)F(z), \\ \rho(x, y, z, t) = \rho_h(x, y, t)G(z) \\ w(x, y, z, t) = w_h(x, y, t)G(z) \end{cases},$$

the equation set (2) can be decomposed into infinitely many shallow-water systems (i.e., an infinite number of vertical

normal modes) with differing equivalent depths ([Majda 2003](#); [Pedlosky 2003](#)). For each vertical mode, the equivalent shallow-water equations are

$$\begin{cases} \frac{\partial u_h}{\partial t} + U \frac{\partial u_h}{\partial x} + V \frac{\partial u_h}{\partial y} - f_0 v_h = -g \frac{\partial \eta}{\partial x} \\ \frac{\partial v_h}{\partial t} + U \frac{\partial v_h}{\partial x} + V \frac{\partial v_h}{\partial y} + f_0 u_h = -g \frac{\partial \eta}{\partial y} \\ \frac{\partial \eta}{\partial t} + U \frac{\partial \eta}{\partial x} + V \frac{\partial \eta}{\partial y} + H_e \left(\frac{\partial u_h}{\partial x} + \frac{\partial v_h}{\partial y} \right) = 0 \end{cases}. \quad (3)$$

The vertical structure $F(z) = \sum_{n=0}^{+\infty} a_n F_n(z)$, with a_n denoting the arbitrary constant, is given by the following eigenvalue problem

$$\begin{aligned} \frac{d}{dz} \left[\left(\frac{1}{N^2} \frac{dF(z)}{dz} \right) \right] + \frac{1}{gH_e} F(z) = 0 \\ \text{subject to boundary conditions } \begin{cases} \left. \frac{dF(z)}{dz} \right|_{z=0} = 0 \\ \left. \frac{dF(z)}{dz} \right|_{z=-H} = 0 \end{cases}, \quad (4) \end{aligned}$$

where H_e is the equivalent depth and H is the ocean depth. Then Fourier transform the equation set (3) and sort it into matrix form

$$\begin{aligned} \begin{bmatrix} i\omega + iUk + iVl & -f_0 & ikg \\ f_0 & i\omega + iUk + iVl & ilg \\ ikH_e & ilH_e & i\omega + iUk + iVl \end{bmatrix} \begin{bmatrix} \widehat{u}_h \\ \widehat{v}_h \\ \widehat{\eta} \end{bmatrix} \\ = \begin{bmatrix} i\Omega & -f_0 & ikg \\ f_0 & i\Omega & ilg \\ ikH_e & ilH_e & i\Omega \end{bmatrix} \begin{bmatrix} \widehat{u}_h \\ \widehat{v}_h \\ \widehat{\eta} \end{bmatrix} = 0, \quad (5) \end{aligned}$$

where a caret ($\widehat{\quad}$) denotes Fourier-transformed variables, ω the frequency, k the zonal wavenumber, l the meridional wavenumber, and $\Omega = \omega + Uk + Vl$ the intrinsic frequency. Nontrivial solutions of the equation set (5) require that

$$\begin{vmatrix} i\Omega & -f_0 & ikg \\ f_0 & i\Omega & ilg \\ ikH_e & ilH_e & i\Omega \end{vmatrix} = \Omega(\Omega^2 - f_0^2 - c^2 K^2) = 0, \quad (6)$$

where $c = \sqrt{gH_e}$, and $K^2 = k^2 + l^2$. Resembling the classic normal-mode decomposition ([Müller 1984, 1988](#); [Lien and Müller 1992](#)), the equation set (6) describes two distinct dynamical modes, with $\Omega = 0$ and $\Omega = \pm \sqrt{f_0^2 + c^2 K^2}$ representing vortical and wavy modes, respectively.

We note that vortical and wavy modes are eigenfunctions which form a complete and orthogonal basis in (x, y) space ([Machenauer 1977](#); [Baer and Tribbia 1977](#); [Leith 1980](#); [Salmon 1988, 1998](#); [Remmel and Smith 2009](#)) such that a linear combination of eigenfunctions constitutes realistic flow regimes such as vortical motions. It is thus necessary to distinguish between vortical modes and vortical motions, especially when the Rossby number is $O(1)$ or larger ([Lien and Müller 1992](#)). When the Rossby number is large enough, vortical and wavy modes are strongly coupled so that it becomes

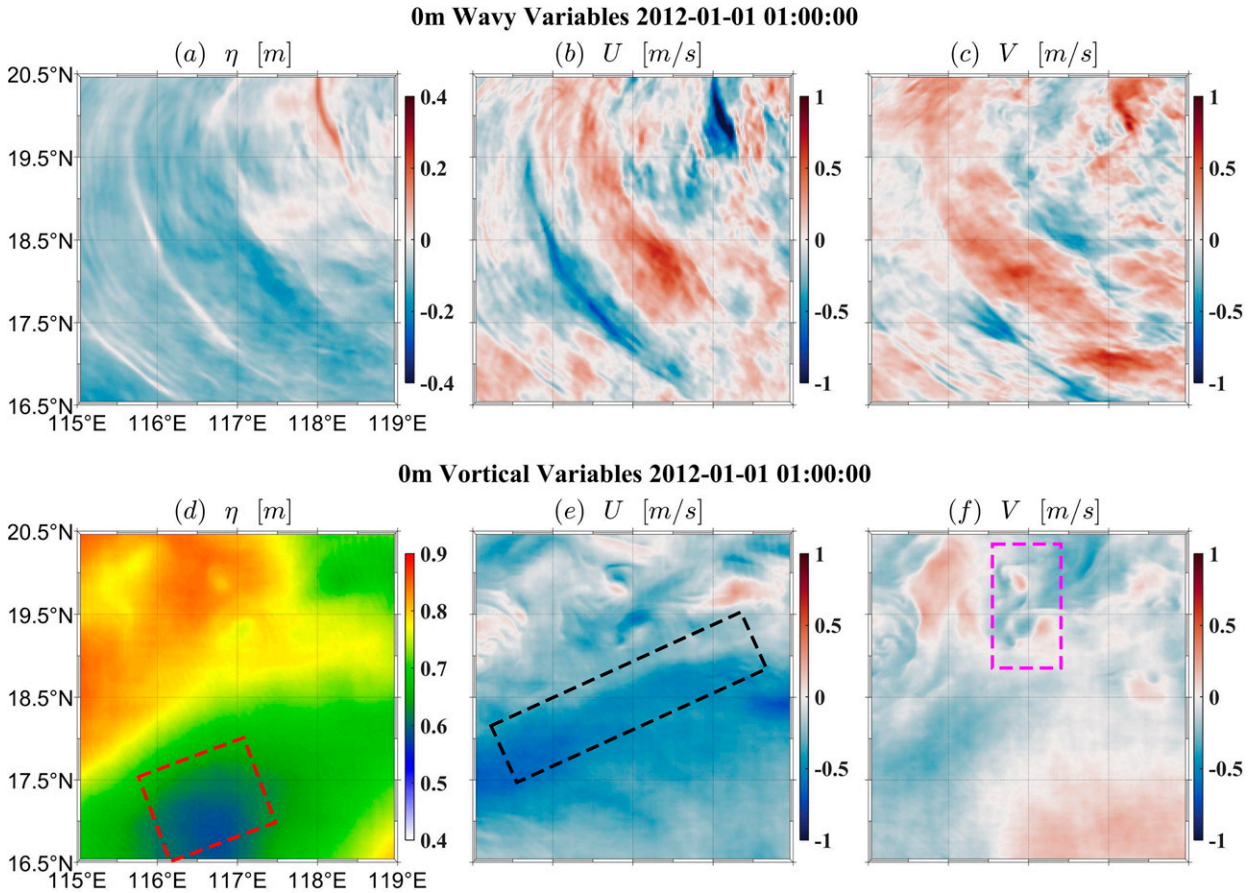


FIG. 1. (a)–(c) Wavy and (d)–(f) vortical (left) sea surface height, (center) zonal velocity, and (right) meridional velocity. The black box in (e), red box in (d), and magenta box in (f) highlight large-scale, mesoscale, and submesoscale features, respectively.

nontrivial to define and distinguish vortical motions. In the following, we seek to propose a working approach for defining and distinguishing vortical and wavy motions, which will vividly show its rationality and usefulness in section 3.

The equation of the vertical component of vorticity can be derived from the equation set (2)

$$\frac{\partial \zeta}{\partial t} + U \frac{\partial \zeta}{\partial x} + V \frac{\partial \zeta}{\partial y} + f_0 \chi = 0, \tag{7}$$

where ζ is the vertical component of the relative vorticity (hereafter referred simply to as the relative vorticity) and $\chi = (\partial u/\partial x) + (\partial v/\partial y)$ is the divergence of the horizontal velocity (hereafter termed as the horizontal divergence). In practice, the following is used to partially consider the β effect,

$$\frac{\partial \zeta}{\partial t} + U \frac{\partial \zeta}{\partial x} + V \frac{\partial \zeta}{\partial y} + f \chi = \frac{\partial \zeta}{\partial t} + U \frac{\partial \zeta}{\partial x} + V \frac{\partial \zeta}{\partial y} + f_{\min} \frac{f \chi}{f_{\min}} = 0, \tag{8}$$

where $f = f_0 + \beta y$ is the Coriolis parameter on the β plane and f_{\min} is the minimum Coriolis parameter in the domain of interest excluding the equatorial regions with vanishing f . The Fourier transform of Eq. (8) gives

$$i\omega \widehat{\zeta} + iUk \widehat{\zeta} + iVl \widehat{\zeta} + f_{\min} \frac{\widehat{f\chi}}{f_{\min}} = i\Omega \widehat{\zeta} + f_{\min} \frac{\widehat{f\chi}}{f_{\min}} = 0, \tag{9}$$

where $\widehat{f\chi}/f_{\min}$ is the modified horizontal divergence that takes the β effect into consideration. Two significant observations immediately follow from Eq. (9): (i) for the vortical modes whose intrinsic frequency is below the inertial frequency, the modulus of the modified horizontal divergence is smaller than that of the relative vorticity; (ii) for the wavy modes whose intrinsic frequency is above the inertial frequency, the modulus of the modified horizontal divergence is larger than that of the relative vorticity. Once the nonlinearity is involved, modal interaction (e.g., wavy–vortical interaction) can generate vortical motions whose dynamical properties are elusive at first sight. However, wavy motions (e.g., barotropic tides and IGWs), basically of linear dynamics, are supposed to have the same dynamical properties as wavy modes and thus are much easier to be defined and isolated. Our strategy in the following is to first define wavy motions, the orthogonal complement of which is then defined as vortical motions (e.g., large-scale circulations, mesoscale flows, and submesoscale flows).

Each point in spectral space [i.e., (k, l, ω)] is in general contributed by a linear combination of vortical and wavy modes;

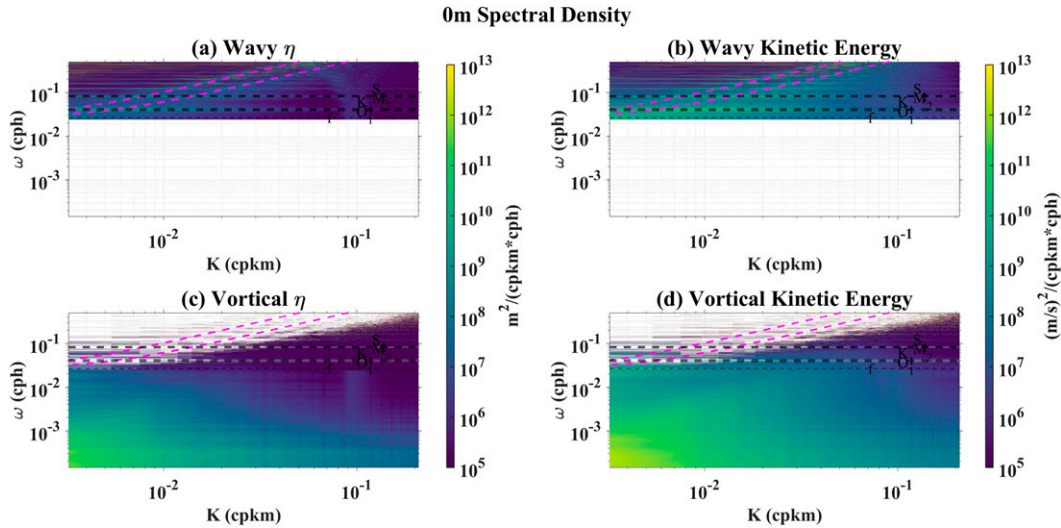


FIG. 2. Frequency–wavenumber spectra of the (a),(c) sea surface height and (b),(d) horizontal kinetic energy associated with (top) wavy and (bottom) vortical motions. The dashed magenta lines denote dispersion relation curves of the first and second baroclinic-mode internal inertial–gravity waves. The dashed black lines show the diurnal (K_1 , O_1), semidiurnal (M_2 , S_2) tidal frequencies, and the inertial frequency in the center of the study region.

therefore, it is reasonable to assume that wherever in spectral space wavy modes dominate, the modulus of the modified horizontal divergence $|\widehat{f\chi}/f_{\min}|$ should be larger than that of the relative vorticity $|\widehat{\zeta}|$. With this in mind, wavy motions can be defined as those with $|\widehat{f\chi}/f_{\min}|$ and $|\Omega|$ being larger than $|\widehat{\zeta}|$ and $|f_{\min}|$, respectively. Naturally, the rest are defined as vortical motions:

- Category 1: $|\widehat{\zeta}| > |\widehat{f\chi}/f_{\min}|$ and $|\Omega| < |f_{\min}|$. Mesoscale motions undoubtedly fall into this category which can also include some low-frequency submesoscale motions (Torres et al. 2018).
- Category 2: $|\widehat{\zeta}| > |\widehat{f\chi}/f_{\min}|$ and $|\Omega| > |f_{\min}|$. High-frequency submesoscale motions (Torres et al. 2018), which are usually rapidly advected by strong meso- and large-scale flows, belong to this category. For example, submesoscale eddies and filaments in the Kuroshio Extension region are typically of high frequency (see section S1 in the online supplemental material).
- Category 3: $|\widehat{\zeta}| < |\widehat{f\chi}/f_{\min}|$ and $|\Omega| < |f_{\min}|$. The low-frequency submesoscale motions (Torres et al. 2018), which are exemplified by submesoscale weakly interacting with weak meso- and large-scale motions, are identified with this category. For example, submesoscale motions in central South China Sea are usually of low frequency (see section S1 in supplemental material).

Mathematically, the above definitions can be concisely summarized as follows:

$$\widehat{M}_v(k, l, \omega) = \begin{cases} 0, & \text{if } |\widehat{\zeta}| < \left| \frac{\widehat{f\chi}}{f_{\min}} \right| \text{ and } |\Omega| > |f_{\min}| \text{ at } (k, l, \omega) \\ 1, & \text{if } |\widehat{\zeta}| > \left| \frac{\widehat{f\chi}}{f_{\min}} \right| \text{ or } |\Omega| < |f_{\min}| \text{ at } (k, l, \omega) \end{cases}, \tag{10}$$

$$\widehat{M}_w(k, l, \omega) = \begin{cases} 1, & \text{if } |\widehat{\zeta}| < \left| \frac{\widehat{f\chi}}{f_{\min}} \right| \text{ and } |\Omega| > |f_{\min}| \text{ at } (k, l, \omega) \\ 0, & \text{if } |\widehat{\zeta}| > \left| \frac{\widehat{f\chi}}{f_{\min}} \right| \text{ or } |\Omega| < |f_{\min}| \text{ at } (k, l, \omega) \end{cases}, \tag{11}$$

where M_v and M_w are filters in physical space [i.e., (x, y, t)] for the vortical and wavy motions, respectively, and the subscript $v(w)$ denotes vortical (wavy) motions. With the filters devised, any physical variable A of the full flow can be decomposed into the vortical (A_v) and wavy (A_w) components,

$$\begin{cases} \widehat{A}_v = \widehat{A} \times \widehat{M}_v \\ \widehat{A}_w = \widehat{A} \times \widehat{M}_w \end{cases}, \tag{12}$$

where \times denotes multiplication. Once the inverse Fourier transforming of the equation set (12) is conducted, the physical-space decomposition is recovered

$$\begin{cases} A_v = M_v * A = \iiint_{\Omega} M_v(\tau_x, \tau_y, \tau_t) \cdot A(x - \tau_x, y - \tau_y, t - \tau_t) d\tau_x d\tau_y d\tau_t \\ A_w = M_w * A = \iiint_{\Omega} M_w(\tau_x, \tau_y, \tau_t) \cdot A(x - \tau_x, y - \tau_y, t - \tau_t) d\tau_x d\tau_y d\tau_t \end{cases}, \tag{13}$$

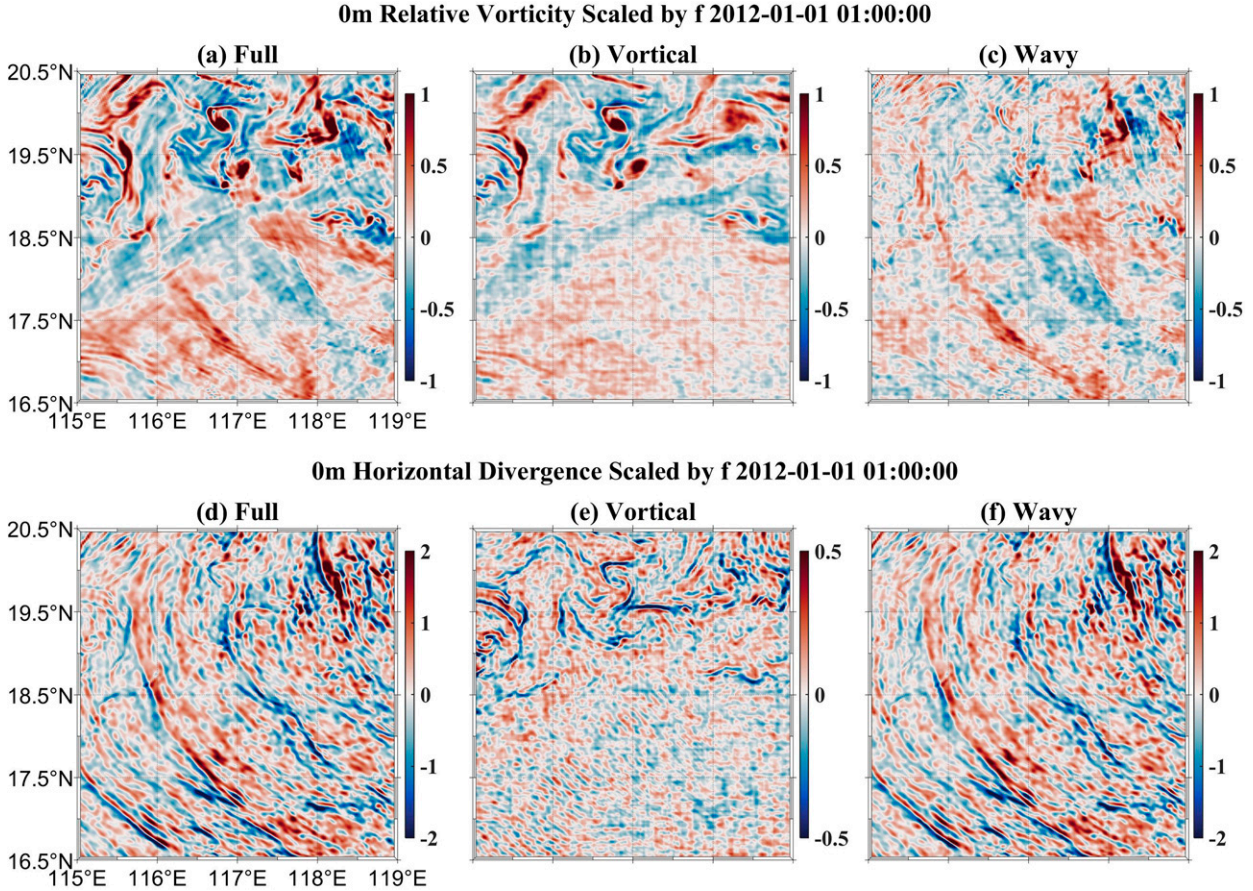


FIG. 3. (a)–(c) Relative vorticity and (d)–(f) horizontal divergence for the (left) full, (center) vortical, and (right) wavy motions. The color scale of (e) is different from that of (d) and (f).

where the $*$ denotes convolution, \mathcal{U} the temporal (i.e., τ_t) and horizontal domain (i.e., τ_x and τ_y) over which the integration is taken. At this point, it is necessary to note the following:

- 1) The spectral filters [i.e., Eqs. (10) and (11)] are of the 0/1 type, meaning that it is assumed that vortical and wavy motions do not occupy the same spectral points. The 0/1-type spectral filters are actually an extension of the Fourier temporal/spatial filter (Frisch 1995) to a dynamics-based spatiotemporal filter; thus, the important property that vortical and wavy motions are orthogonal in the space L^2 (i.e., $\iint_{\mathcal{U}} A_v^2 dx dy dt + \iint_{\mathcal{U}} A_w^2 dx dy dt = \iint_{\mathcal{U}} A^2 dx dy dt$) is inherited from the Fourier filtering, which guarantees the physical validity of the decomposition (Bucciotti et al. 2021). Note that the proposed filtering is also a generalization of the Leonard filtering which has recently been used in the oceanographic community (e.g., Aluie et al. 2018; Schubert et al. 2020) to perform temporal/spatial-scale decomposition.
- 2) The Fourier transform, based on which the spectral filters are designed, is inherently unable to retain local space–time information; therefore, if a point in spectral space is determined to be the vortical (wavy) motion by the filters, then every point in physical space that corresponds to that spectral point will be designated as the vortical (wavy) motion.

Importantly, convolving the equation set (1) with the filter for vortical (wavy) motions and utilizing the important property that convolution commutes with differentiation, we can derive the governing equations for the vortical (wavy) motions. For example, the governing equations for vortical motions are

$$\begin{cases} \frac{\partial u_v}{\partial t} + \frac{\partial(uu)_v}{\partial x} + \frac{\partial(vu)_v}{\partial y} + \frac{\partial(wu)_v}{\partial z} - (fv)_v = -\frac{1}{\rho_0} \frac{\partial p_v}{\partial x} + S_v^u \\ \frac{\partial v_v}{\partial t} + \frac{\partial(uv)_v}{\partial x} + \frac{\partial(vv)_v}{\partial y} + \frac{\partial(wv)_v}{\partial z} + (fu)_v = -\frac{1}{\rho_0} \frac{\partial p_v}{\partial y} + S_v^v \\ \frac{\partial p_v}{\partial z} = -\rho_v g \\ \frac{\partial u_v}{\partial x} + \frac{\partial v_v}{\partial y} + \frac{\partial w_v}{\partial z} = 0 \\ \frac{\partial \rho_v}{\partial t} + \frac{\partial(u\rho)_v}{\partial x} + \frac{\partial(v\rho)_v}{\partial y} + \frac{\partial(w\rho)_v}{\partial z} - \frac{\rho_0}{g} (wN^2)_v = S_v^p \end{cases}, \quad (14)$$

where the β plane is invoked and subgrid terms (i.e., S^u , S^v , and S^p) are restored for completeness. Replacing the subscript with w gives the governing equations for wavy motions. Recall that vortical motions in the ocean include large-scale circulations, mesoscale flows and submesoscale flows, whereas wavy motions involve mainly barotropic tides and IGWs.

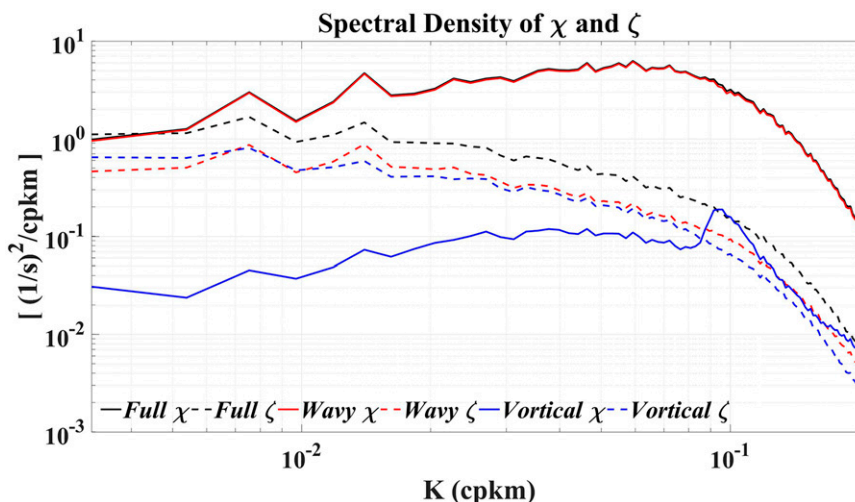


FIG. 4. Wavenumber spectra of horizontal divergence (solid lines) and relative vorticity (dashed lines) for the full flows (black lines), wavy motions (red lines), and vortical motions (blue lines). The wavenumber spectra are obtained through frequency-wise integration of corresponding frequency–wavenumber spectra like Fig. 2.

In summary, we have managed to decompose both the variables and primitive equations of the full flow into vortical and wavy regimes, mainly based on the relative magnitudes of the relative vorticity and the modified horizontal divergence in spectral space.

3. Application

As a proof of concept, we apply the proposed methodology to a $4^\circ \times 4^\circ$ subdomain ($16.5^\circ\text{--}20.5^\circ\text{N}$, $115^\circ\text{--}119^\circ\text{E}$) from the central South China Sea, utilizing the hourly model outputs from a global, tide-resolving and submesoscale-admitting configuration (i.e., LLC4320) of the MITgcm. Because the full luni-solar tidal potential is included as forcing in the LLC4320 simulation, the IGW continuum is partially resolved in the simulated flow. Readers are referred to Arbic et al. (2018) and https://www.cvs.mitgcm.org/viewvc/MITgcm/MITgcm_contrib/llc_hires/ for more details about the LLC4320 simulation. Before results are presented, several technical details are clarified:

- When the Fourier transform is performed, neither tapering windows are imposed (Smith 2008; Zhao et al. 2019; Zhao 2020, 2021; Gong et al. 2021) nor linear trends are removed (Torres et al. 2019; Zhao et al. 2019; Gong et al. 2021; Zhao 2020, 2021). In fact, we found that the decomposed results, with or without tapering/detrending, are essentially the same (see section S2 in the supplemental material).
- Since the intrinsic frequency Ω is not known a priori, Ω in Eqs. (10) and (11) is simply replaced with ω as a compromise. This, in this step, effectively neglects the advection effect by the background flow.
- The decomposed vortical and wavy motions, obtained via Eqs. (10) and (11), are already satisfactory except that vortical motions artificially present spectral peaks exactly at the four predominant tidal frequencies (i.e., K_1 , O_1 , M_2 , S_2)

(see section S3 in the supplemental material). To remedy this, Eqs. (10) and (11) are readily improved as follows

$$\widehat{M}_v(k, l, \omega) = \begin{cases} 0, & \text{if } \left(|\widehat{\zeta}| < \left| \frac{\widehat{f\chi}}{f_{\min}} \right| \text{ and } |\omega| > |f_{\min}| \right) \\ & \text{or } (\omega = \omega_{\text{tide}}) \text{ at } (k, l, \omega) \\ 1, & \text{if } \left(|\widehat{\zeta}| > \left| \frac{\widehat{f\chi}}{f_{\min}} \right| \text{ or } |\omega| < |f_{\min}| \right) \\ & \text{and } (\omega \neq \omega_{\text{tide}}) \text{ at } (k, l, \omega) \end{cases}, \quad (15)$$

$$\widehat{M}_w(k, l, \omega) = \begin{cases} 1, & \text{if } \left(|\widehat{\zeta}| < \left| \frac{\widehat{f\chi}}{f_{\min}} \right| \text{ and } |\omega| > |f_{\min}| \right) \\ & \text{or } (\omega = \omega_{\text{tide}}) \text{ at } (k, l, \omega) \\ 0, & \text{if } \left(|\widehat{\zeta}| > \left| \frac{\widehat{f\chi}}{f_{\min}} \right| \text{ or } |\omega| < |f_{\min}| \right) \\ & \text{and } (\omega \neq \omega_{\text{tide}}) \text{ at } (k, l, \omega) \end{cases}, \quad (16)$$

where ω_{tide} represents the frequencies of the four predominant tidal constituents.

a. Decomposed oceanic variables

We now demonstrate usefulness of the proposed methodology with the decomposed variables. Figure 1 shows wavy and vortical variables (i.e., sea surface height and horizontal velocities). As expected, wavy variables (Figs. 1a–c) display evident baroclinic tides (i.e., internal tides) southwestward propagating from the Luzon Strait. Barotropic tides, with a large-scale pattern, are present in the wavy sea surface height (Fig. 1a) but less identifiable in horizontal velocities (Figs. 1b,c) where barotropic tidal velocities are overwhelmed by internal tidal velocities. Wavy motions are well constrained by wavy dynamics as shown in the frequency–wavenumber spectra (Figs. 2a,b)

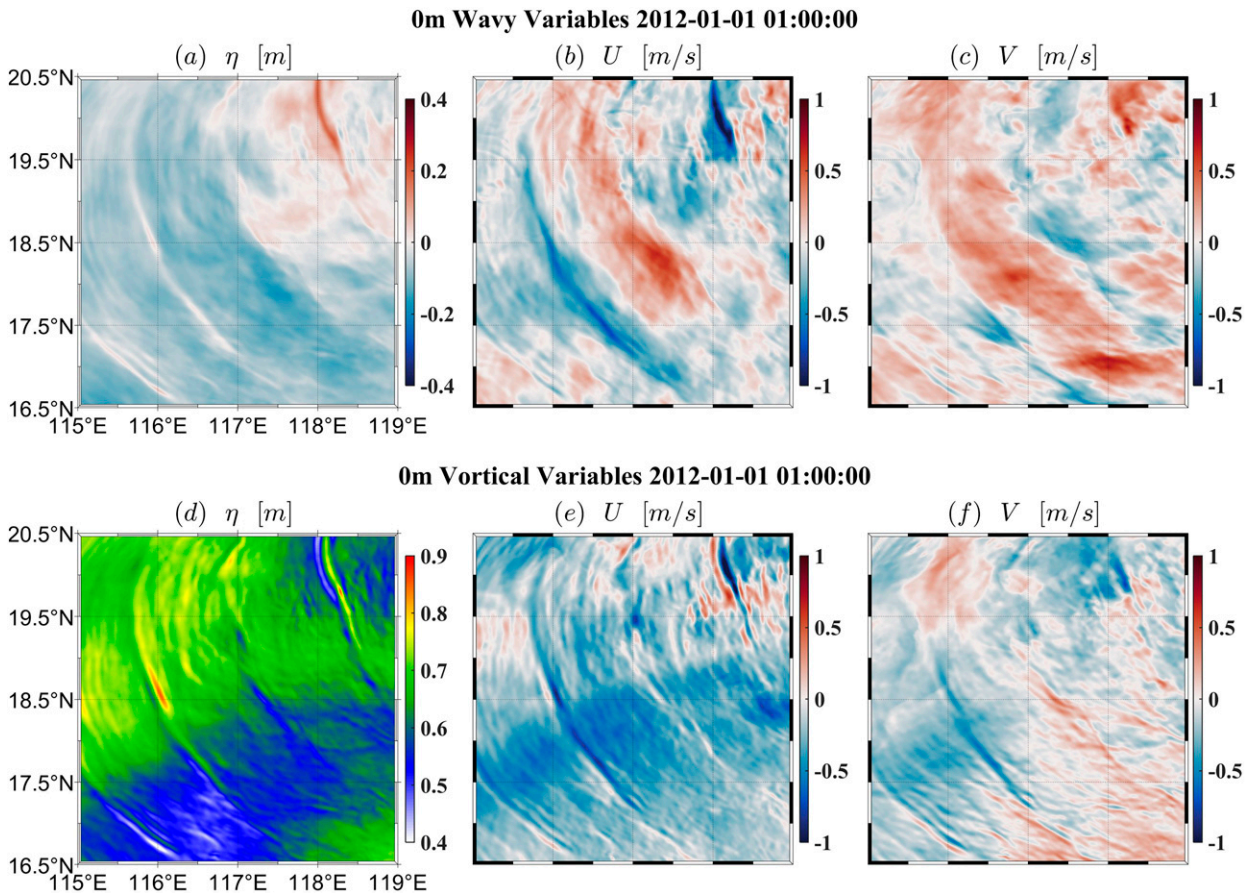


FIG. 5. As in Fig. 1, but using Lagrangian filtering.

where most energies are concentrated along tidal frequencies and the dispersion relation curves of mode-1 and mode-2 IGWs. By contrast, vortical motions (Figs. 1d–f) are much weaker. They are characterized by prototypical large-scale currents which flows southwestward (highlighted by the black box in Fig. 1e), mesoscale features (e.g., a weak cyclonic mesoscale eddy emphasized by the red box in Fig. 1d) and submesoscale structures (e.g., two cyclonic submesoscale eddies highlighted by the magenta box in Fig. 1f). Correspondingly, spectral energies of vortical motions (Figs. 2c,d), obviously with wavy energies removed, are mostly of subinertial nature. In particular, the relative vorticity of the full flow (Fig. 3a) more clearly demonstrates abundant submesoscale features (e.g., filaments and eddies with high relative vorticity) which are, however, obscured by the strong horizontal divergence of IGWs in the full flow (Fig. 3d). The extracted vortical motions satisfactorily recover those submesoscale features as patches with large relative vorticity (Fig. 3b) and significant horizontal divergence (Fig. 3e). As shown by the wavenumber spectra of the relative vorticity and horizontal divergence (Fig. 4), the horizontal divergence of vortical motions is even stronger than the relative vorticity at scales below ~ 12 km, in agreement with previous studies such as Barkan et al. (2019), who stressed the importance of horizontal divergence during submesoscale frontogenesis. Therefore, although our filter for vortical motions [i.e., Eq. (15)]

constrains the magnitude of the relative vorticity to be larger than the modified horizontal divergence in spectral space, the decomposed vortical motions in physical space manage to reveal submesoscale processes having nonnegligible horizontal divergence. Comparatively, wavy motions have much larger horizontal divergence than the relative vorticity at all the resolved spatial scales (Figs. 3c,f and 4); constrained by leading-order dynamics of IGWs, such discrepancy increases with the increasing wavenumber (Fig. 4) which in turn means the increasing frequency according to the dispersion relation. Note that the dashed red and blue lines in Fig. 4 indicate that the relative vorticity of wavy motions can be as large as that of vortical motions and thus are nonnegligible irrespective of spatial scales of interest. This is an important observation, and one should expect that this is especially true in oceanic regions where internal tides are vigorous but mesoscale activities are weak.

b. Comparison with Lagrangian filtering

Lagrangian filtering intends to separate wavy motions from nonwavy motions and has recently attracted much attention (Bachman et al. 2020; Shakespeare et al. 2021). For comparison, the decomposition of the same flow using Lagrangian filtering is shown in Fig. 5. For the parameter settings in the Python package Lagrangian filtering, the particle-tracking window is ± 2 days as suggested by Shakespeare et al. (2021);

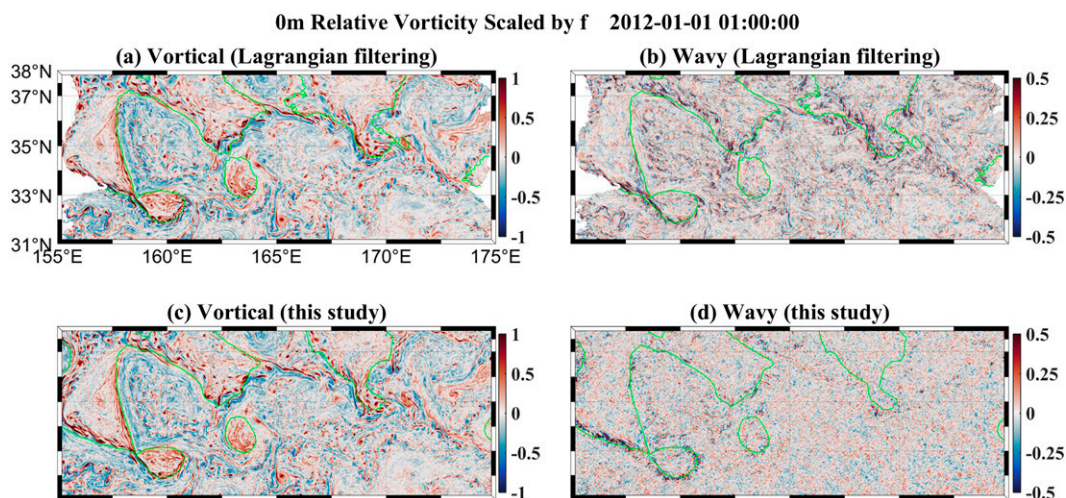


FIG. 6. Relative vorticity of (a),(c) vortical and (b),(d) wavy motions which are decomposed using (top) Lagrangian filtering and (bottom) our methodology. Green curves denote the 0.5-m contours of vortical sea surface height that roughly represents the Kuroshio Extension streamline.

the particle-tracking time step is 25 s, which is the same as the time-marching step of the LLC4320 simulation; a fourth-order Butterworth filter, which is the default setting, is used; the cutoff frequency is the inertial frequency at 10°N which is smaller

than the minimum latitude (i.e., 16.5°) of the study region and this choice of the cutoff frequency intends to extract IGWs as completely as possible. An auxiliary comparison is also made in the Kuroshio Extension region (Fig. 6); all parameters for

Full Motions (10^{-4} m/s^2) at 0m 2012-01-01 01:00:00

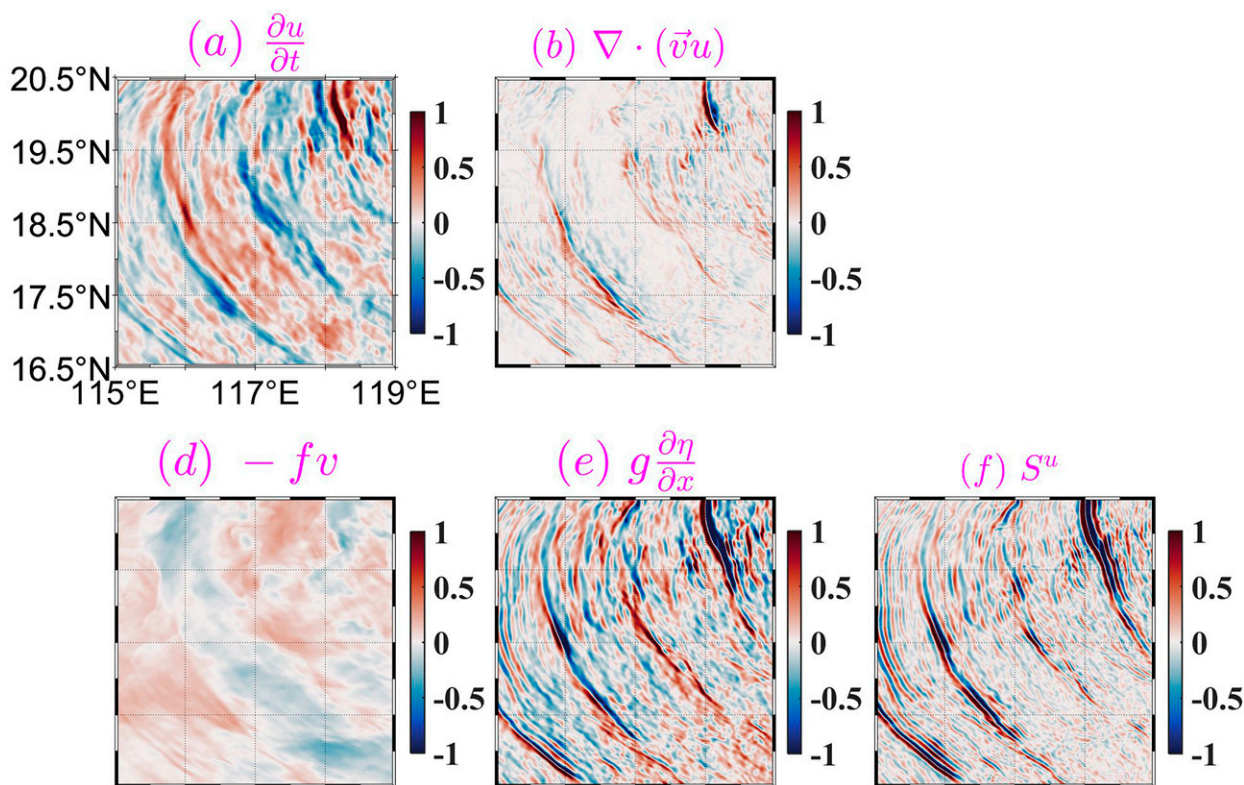


FIG. 7. Individual terms of the zonal momentum equation governing the full flow. The (a) time derivative, (b) advective term, (d) Coriolis term, (e) pressure gradient term, and (f) residual term are displayed.

Wavy Motions (10^{-4} m/s^2) at 0m 2012-01-01 01:00:00

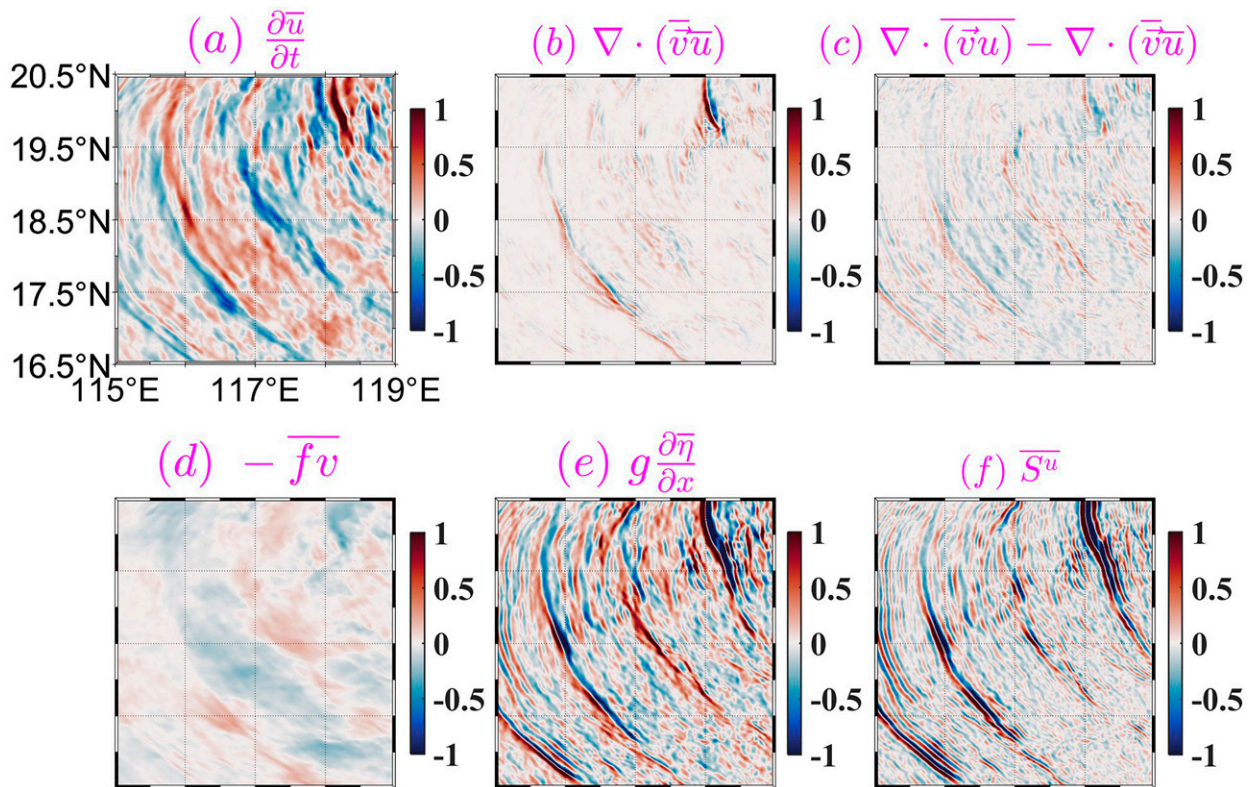


FIG. 8. Individual terms of the zonal momentum equation governing the wavy motions. The (a) time derivative, (b) self-interaction term, (c) interaction with vortical motions, (d) Coriolis force, (e) pressure gradient term, and (f) residual term are displayed. The overbar denotes convolved variables with the filter for wavy motions.

Lagrangian filtering are the same as in the central South China except that the cutoff frequency is the inertial frequency at 40°N which is larger than the maximum latitude (i.e., 38°) of the Kuroshio Extension region and this choice of the cutoff frequency intends to extract IGWs as purely as possible.

Two important observations are clear from the comparisons. First of all, vortical variables obtained from Lagrangian filtering (Figs. 5d–f) contain obvious propagating internal tides which are not visible in vortical variables (Figs. 1d–f) decomposed using our methodology. Given that wavy and vortical motions sum to the full flow by definition, at least for the case considered here, Lagrangian filtering does not fully extract wavy motions (Figs. 5a–c). Second, vortical motions from Lagrangian filtering (Fig. 6a) and our methodology (Fig. 6c) consistently reveal an abundance of mesoscale and submesoscale processes along the Kuroshio Extension streamline. However, many filamentlike submesoscale structures, especially those distributed along the Kuroshio Extension streamline, manifest themselves in the relative vorticity of wavy motions by Lagrangian filtering (Fig. 6b), but not in that by our methodology (Fig. 6d). This suggests that some vortical motions (e.g., high-frequency submesoscale flows) are unfortunately attributed to wavy motions by Lagrangian filtering.

We can thus conclude that our methodology does seem to be valid and efficient in distinguishing between wavy and vortical motions. By contrast, when it is necessary to extract the ageostrophic motion as a whole, which includes not only IGWs but also high-frequency submesoscale flows, Lagrangian filtering should be effective.

c. Decomposed momentum equations

We now proceed to examine the momentum balance of the full and decomposed flows. Figure 7 shows spatial distributions of each individual term of the zonal momentum equation governing the full flow. Generally, the time derivative, Coriolis term, and pressure gradient term are dominant. The three-term balance corresponds to strong IGWs and barotropic tides in the study region. The nonlinear advective term is much weaker for the most part but remains significant for small-scale IGWs. From Fig. 7, it is difficult to identify the momentum balance for vortical motions which are overwhelmed by energetic IGWs. With our dynamics-based decomposition applied, the zonal momentum equations of wavy and vortical motions can be readily separated and are anatomized here in Figs. 8 and 9, respectively. The evolution of wavy motions is governed primarily by the time derivative,

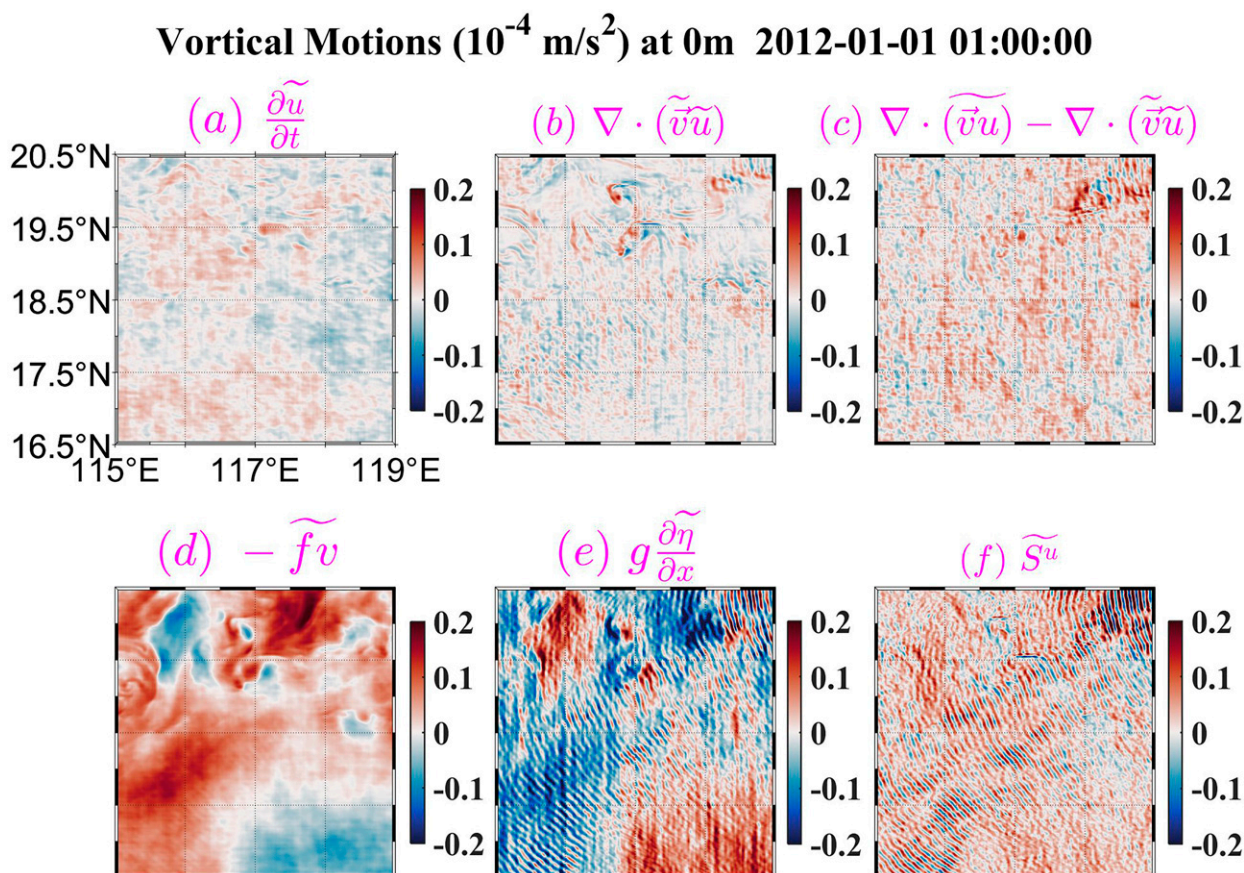


FIG. 9. Individual terms of the zonal momentum equation governing the vortical motions. The (a) time derivative, (b) self-interaction term, (c) interaction with the wavy motions, (d) Coriolis term, (e) pressure gradient term, and (f) residual term are displayed. The tilde denotes convolved variables with the filter for vortical motions.

Coriolis force, and the pressure gradient force, with the non-linear advective term playing a role at small scales. Vortical motions are predominantly in geostrophic balance, with typical examples including the already mentioned large-scale current and cyclonic mesoscale eddy. Also note the intense self-interaction of the two cyclonic submesoscale eddies mentioned in section 3a (Fig. 9b). Unfortunately, Figs. 9e and 9f artificially display wavelike stripes. This is the well-known Gibbs phenomenon in the Fourier-transform-based filtering that uses the spectral-cutoff-type filter [e.g., Eqs. (15) and (16)]. We will further discuss this phenomenon in section 4. Overall, characteristics revealed by the decomposed wavy and vortical motions agree well with diagnostics of the governing equations for the full flow. The meridional momentum equations demonstrate similar characteristics and are not presented.

4. Discussion and summary

In this study, we have proposed a simple methodology for decomposing oceanic flows into vortical and wavy regimes by virtue of their contrasting dynamical characteristics. We offer a preliminary demonstration of its validity and efficiency with a proof-of-concept application to the central South China

Sea. To further test usefulness of the methodology, we have also performed the decomposition over the whole South China Sea, assuming that values over land and islands are zeros (Smith 2008; Gong et al. 2021). The decomposed wavy variables (Figs. 10a–c) satisfactorily recover strong barotropic and baroclinic tides; the decomposed vortical variables (Figs. 10d–f) successfully reveal prototypical large-scale and mesoscale features including the Kuroshio intrusion into the South China Sea, the western boundary current along the Vietnam coast and the anticyclonic mesoscale eddy southwest of the Taiwan Island. Importantly, we have compared the decomposed results over the whole South China Sea with those over the abovementioned $4^\circ \times 4^\circ$ subdomain from the central South China Sea ($16.5^\circ\text{--}20.5^\circ\text{N}$, $115^\circ\text{--}119^\circ\text{E}$) and found that the differences are negligibly small (see section S4 in supplemental material). All those indicate that the proposed decomposition methodology seems to also work in the presence of complex coastal geometry.

Previous studies explored the frequency–wavenumber spectra of LLC4320 variables (e.g., sea surface height, sea surface velocities) through breaking the global ocean into small (e.g., $5^\circ \times 5^\circ$) boxes (Qiu et al. 2018; Torres et al. 2018). Based on the success of this box-based trick, the applicability of the

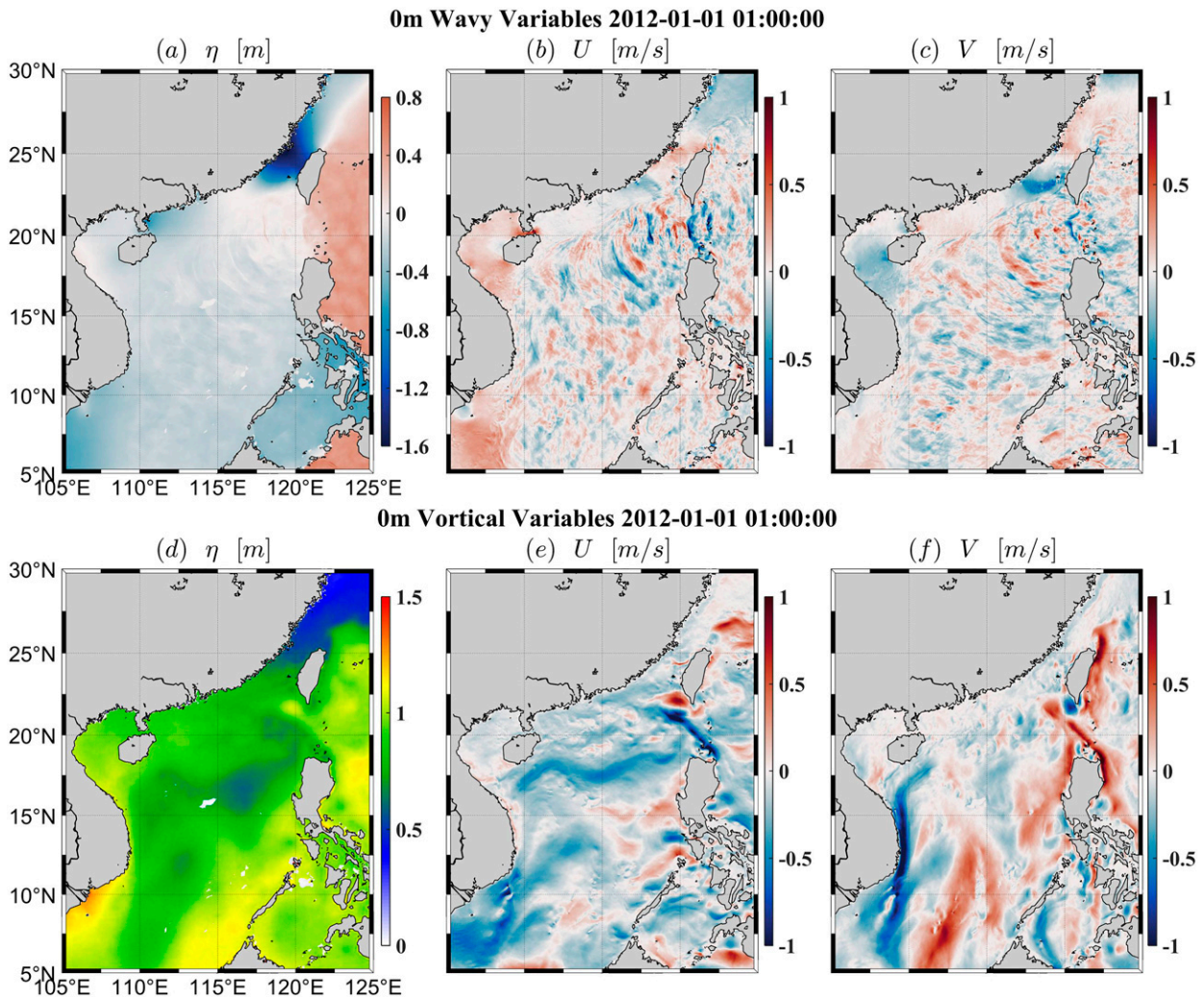


FIG. 10. As in Fig. 1, but for the whole South China Sea.

proposed methodology to the global ocean simulation is anticipated. Used jointly with conventional time-scale or space-space decompositions (e.g., Frisch 1995; Aluie et al. 2018; Liang 2016), our dynamics-based methodology will help resolve the challenging problem of multiscale interactions and associated energy transfers over the global ocean. And for ever-popular global high-resolution simulations with explicit tidal forcing, an online decomposition of the vortical and wavy motions would facilitate parameterization of both isopycnal mixing (eddy flux) essentially due to vortical motions and diapycnal mixing mainly arising from IGW breaking.

While the proposed methodology shows clear usefulness, some caveats require attention. First of all, the decomposition builds its theoretical and methodological basis on the Fourier transform. Therefore, it inherits classical concerns about the Fourier transform. Most importantly, although 0/1-type spectral filters [e.g., Eqs. (15) and (16)] are commonly used in turbulence studies (Frisch 1995) and are recently employed in oceanographic research (Torres et al. 2019), they induce the

Gibbs phenomenon. For the simple low-pass or high-pass filtering, the Gibbs phenomenon can be attenuated through smoothly rather than abruptly decreasing values of spectral filters from 1 to 0. However, this manner of alleviating the Gibbs phenomenon is less hopeful for the dynamics-based spectral filter [i.e., Eqs. (15) and (16)] which has a complicated 0/1 distribution. Presently, there seems to be no perfect way out. Moreover, homogeneity of the flows is implicitly assumed as the Fourier transform is inherently unable to retain local space-time information. This does not seem to be a serious problem as shown by physically reasonable decomposed results in the whole South China Sea.

Second, the assumption that vortical and wavy motions are mutually exclusive in spectral space is introduced in the decomposition. Both barotropic tides and low-mode IGWs are basically of linear nature and their dynamics are strongly constrained by dispersion relations. Large-scale circulations and mesoscale flows are of low frequency. Therefore, large-scale circulation and mesoscale flows, most probably, do not occupy

the same spectral points with barotropic tides or low-mode IGWs. It is, however, possible that high-mode IGWs and submesoscale flows can have overlaps in spectral space (McWilliams 2016), which is an extremely complicated scenario. When vortical and wavy motions are allowed to overlap in spectral space, it is highly possible that the orthogonality property gets impaired. In addition, the separating and coupling between high-mode IGWs and submesoscale flows are community-challenging issues (McWilliams 2016) and are presently difficult to unambiguously tackle. By assuming that vortical and wavy motions do not overlap in spectral space, we have reached a working decomposition methodology that yields physically sensible results in oceanic regions with contrasting dynamics. Further improvement of the proposed decomposition is anticipated in the future.

Third, the proposed methodology would fail in the equatorial regions because of the peculiarity of ocean dynamics there.

Fourth, it is difficult to directly apply our decomposition to current observational data (e.g., moored/transect observations, satellite altimeter data) since the methodology requires input data to be three-dimensional (i.e., latitudinal, longitudinal, temporal) and frequent enough to resolve IGWs.

Last, for the application on the non- β plane (e.g., an extremely large domain which renders the β -plane approximation invalid), one trick is to break the large domain into many small boxes to meet the β -plane approximation. Another way is to generalize the proposed filters and associated convolution from the Cartesian system to the spherical system (e.g., Aluie 2019).

Acknowledgments. This work was supported by the National Natural Science Foundation of China (91858201, 42076013, 92258301, and 41721005) and the Natural Science Foundation of Fujian Province of China (2021J02005 and 2019J05009). Angus Gibson and Callum Shakespeare from Australian National University are thanked for their helps in the installation of the Python package Lagrangian filtering (<https://github.com/angus-g/lagrangian-filtering>). The authors thank Robin Robertson of Xiamen University Malaysia for helping polish the presentation of this paper. The constructive feedback from two anonymous reviewers greatly improved this paper.

Data availability statement. The LLC4320 simulation output is available at https://data.nas.nasa.gov/ecco/data.php?dir=eccodata/llc_4320. The scripts developed in this study are available at <https://doi.org/10.5281/zenodo.7588212>.

REFERENCES

- Aluie, H., 2019: Convolutions on the sphere: Commutation with differential operators. *Int. J. Geomath.*, **10**, 9, <https://doi.org/10.1007/s13137-019-0123-9>.
- , M. Hecht, and G. K. Vallis, 2018: Mapping the energy cascade in the North Atlantic Ocean: The coarse-graining approach. *J. Phys. Oceanogr.*, **48**, 225–244, <https://doi.org/10.1175/JPO-D-17-0100.1>.
- Arbic, B. K., and Coauthors, 2018: A primer on global internal tide and internal gravity wave continuum modeling in HYCOM and MITgcm. *New Frontiers in Operational Oceanography*, GODAE OceanView, 307–392.
- Bachman, S. D., C. J. Shakespeare, J. Kleypas, F. S. Castruccio, and E. Curchitser, 2020: Particle-based Lagrangian filtering for locating wave-generated thermal refugia for coral reefs. *J. Geophys. Res. Oceans*, **125**, e2020JC016106, <https://doi.org/10.1029/2020JC016106>.
- Baer, F., and J. J. Tribbia, 1977: On complete filtering of gravity modes through nonlinear initialization. *Mon. Wea. Rev.*, **105**, 1536–1539, [https://doi.org/10.1175/1520-0493\(1977\)105<1536:OCFOGM>2.0.CO;2](https://doi.org/10.1175/1520-0493(1977)105<1536:OCFOGM>2.0.CO;2).
- Barkan, R., K. B. Winters, and J. C. McWilliams, 2017: Stimulated imbalance and the enhancement of eddy kinetic energy dissipation by internal waves. *J. Phys. Oceanogr.*, **47**, 181–198, <https://doi.org/10.1175/JPO-D-16-0117.1>.
- , M. J. Molemaker, K. Srinivasan, J. C. McWilliams, and E. A. D'Asaro, 2019: The role of horizontal divergence in submesoscale frontogenesis. *J. Phys. Oceanogr.*, **49**, 1593–1618, <https://doi.org/10.1175/JPO-D-18-0162.1>.
- , K. Srinivasan, L. Yang, J. C. McWilliams, J. Gula, and C. Vic, 2021: Oceanic mesoscale eddy depletion catalyzed by internal waves. *Geophys. Res. Lett.*, **48**, e2021GL094376, <https://doi.org/10.1029/2021GL094376>.
- Buzzicotti, M., B. A. Storer, S. M. Griffies, and H. Aluie, 2021: A coarse-grained decomposition of surface geostrophic kinetic energy in the global ocean. arXiv, 2106.04157v1, <https://doi.org/10.48550/arXiv.2106.04157>.
- Frisch, U., 1995: *Turbulence: The Legacy of A. N. Kolmogorov*. Cambridge University Press, 296 pp.
- Gent, P. R., and J. C. McWilliams, 1990: Isopycnal mixing in ocean circulation models. *J. Phys. Oceanogr.*, **20**, 150–155, [https://doi.org/10.1175/1520-0485\(1990\)020<0150:IMIOCM>2.0.CO;2](https://doi.org/10.1175/1520-0485(1990)020<0150:IMIOCM>2.0.CO;2).
- Gong, Y., M. D. Rayson, N. L. Jones, and G. N. Ivey, 2021: Directional decomposition of internal tides propagating from multiple generation sites. *Ocean Modell.*, **162**, 101801, <https://doi.org/10.1016/j.ocemod.2021.101801>.
- Griffies, S. M., 1998: The Gent–McWilliams skew flux. *J. Phys. Oceanogr.*, **28**, 831–841, [https://doi.org/10.1175/1520-0485\(1998\)028<0831:TGMFSF>2.0.CO;2](https://doi.org/10.1175/1520-0485(1998)028<0831:TGMFSF>2.0.CO;2).
- Jayne, S. R., 2009: The impact of abyssal mixing parameterizations in an ocean general circulation model. *J. Phys. Oceanogr.*, **39**, 1756–1775, <https://doi.org/10.1175/2009JPO4085.1>.
- Leith, C. E., 1980: Nonlinear normal mode initialization and quasi-geostrophic theory. *J. Atmos. Sci.*, **37**, 958–968, [https://doi.org/10.1175/1520-0469\(1980\)037<0958:NNMIAQ>2.0.CO;2](https://doi.org/10.1175/1520-0469(1980)037<0958:NNMIAQ>2.0.CO;2).
- Liang, X. S., 2016: Canonical transfer and multiscale energetics for primitive and quasigeostrophic atmospheres. *J. Atmos. Sci.*, **73**, 4439–4468, <https://doi.org/10.1175/JAS-D-16-0131.1>.
- Lien, R.-C., and P. Müller, 1992: Normal-mode decomposition of small-scale oceanic motions. *J. Phys. Oceanogr.*, **22**, 1583–1595, [https://doi.org/10.1175/1520-0485\(1992\)022<1583:NMDOSS>2.0.CO;2](https://doi.org/10.1175/1520-0485(1992)022<1583:NMDOSS>2.0.CO;2).
- Machenhauer, B., 1977: On the dynamics of gravity oscillations in a shallow water model, with application to normal mode initialization. *Beiträge Phys. Atmos.*, **50**, 253–271.
- Majda, A., 2003: *Introduction to PDEs and Waves for the Atmosphere and Ocean*. Courant Lecture Notes, Vol. 9, Courant Institute of Mathematical Sciences, 234 pp.
- McComas, C. H., and P. Müller, 1981: The dynamic balance of internal waves. *J. Phys. Oceanogr.*, **11**, 970–986, [https://doi.org/10.1175/1520-0485\(1981\)011<0970:TDBOIV>2.0.CO;2](https://doi.org/10.1175/1520-0485(1981)011<0970:TDBOIV>2.0.CO;2).

- McWilliams, J. C., 2016: Submesoscale currents in the ocean. *Proc. Roy. Soc.*, **472A**, 20160117, <https://doi.org/10.1098/rspa.2016.0117>.
- Müller, P., 1984: Small-scale vortical motions. *Internal Gravity Waves Small-Scale Turbulence: Proc. 'Aha Huliko'a Hawaiian Winter Work*. Honolulu, HI, University of Hawai'i at Mānoa, 249–262.
- , 1988: Vortical motions. *Small-Scale Turbulence and Mixing in the Ocean*, J. C. J. Nihoul and B. M. Jamart, Eds., Elsevier Oceanography Series, Vol. 46, Elsevier, 285–301.
- Nagai, T., A. Tandon, E. Kunze, and A. Mahadevan, 2015: Spontaneous generation of near-inertial waves by the Kuroshio front. *J. Phys. Oceanogr.*, **45**, 2381–2406, <https://doi.org/10.1175/JPO-D-14-0086.1>.
- Naviera Garabato, A. C., X. Yu, J. Callies, R. Barkan, K. L. Polzin, E. E. Frajka-Williams, C. E. Buckingham, and S. M. Griffies, 2022: Kinetic energy transfers between mesoscale and submesoscale motions in the open ocean's upper layers. *J. Phys. Oceanogr.*, **52**, 75–97, <https://doi.org/10.1175/JPO-D-21-0099.1>.
- Pedlosky, J., 2003: *Waves in the Ocean and Atmosphere*. Springer, 264 pp.
- Polzin, K. L., and Y. V. Lvov, 2011: Toward regional characterizations of the oceanic internal wavefield. *Rev. Geophys.*, **49**, RG4003, <https://doi.org/10.1029/2010RG000329>.
- Qiu, B., S. Chen, P. Klein, J. Wang, H. Torres, L.-L. Fu, and D. Menemenlis, 2018: Seasonality in transition scale from balanced to unbalanced motions in the World Ocean. *J. Phys. Oceanogr.*, **48**, 591–605, <https://doi.org/10.1175/JPO-D-17-0169.1>.
- Rommel, M., and L. Smith, 2009: New intermediate models for rotating shallow water and an investigation of the preference for anticyclones. *J. Fluid Mech.*, **635**, 321–359, <https://doi.org/10.1017/S0022112009007897>.
- Salmon, R., 1988: Semigeostrophic theory as a Dirac-bracket projection. *J. Fluid Mech.*, **196**, 345–358, <https://doi.org/10.1017/S0022112088002733>.
- , 1998: *Lectures on Geophysical Fluid Dynamics*. Oxford University Press, 378 pp.
- Schubert, R., J. Gula, R. J. Greatbatch, B. Baschek, and A. Biastoch, 2020: The submesoscale kinetic energy cascade: Mesoscale absorption of submesoscale mixed layer eddies and frontal downscale fluxes. *J. Phys. Oceanogr.*, **50**, 2573–2589, <https://doi.org/10.1175/JPO-D-19-0311.1>.
- Scott, R. B., and F. Wang, 2005: Direct evidence of an oceanic inverse kinetic energy cascade from satellite altimetry. *J. Phys. Oceanogr.*, **35**, 1650–1666, <https://doi.org/10.1175/JPO2771.1>.
- Shakespeare, C. J., and A. M. Hogg, 2017: Spontaneous surface generation and interior amplification of internal waves in a regional-scale ocean model. *J. Phys. Oceanogr.*, **47**, 811–826, <https://doi.org/10.1175/JPO-D-16-0188.1>.
- , and —, 2019: On the momentum flux of internal tides. *J. Phys. Oceanogr.*, **49**, 993–1013, <https://doi.org/10.1175/JPO-D-18-0165.1>.
- , A. H. Gibson, A. M. Hogg, S. D. Bachman, S. R. Keating, and N. Velzeboer, 2021: A new open source implementation of Lagrangian filtering: A method to identify internal waves in high-resolution simulations. *J. Adv. Model. Earth Syst.*, **13**, e2021MS002616, <https://doi.org/10.1029/2021MS002616>.
- Smith, J. A., 2008: Vorticity and divergence of surface velocities near shore. *J. Phys. Oceanogr.*, **38**, 1450–1468, <https://doi.org/10.1175/2007JPO3865.1>.
- St. Laurent, L. C., H. L. Simmons, and S. R. Jayne, 2002: Estimating tidally driven mixing in the deep ocean. *Geophys. Res. Lett.*, **29**, 2106, <https://doi.org/10.1029/2002GL015633>.
- Storer, B. A., M. Buzziotti, H. Khatri, S. M. Griffies, and H. Aluie, 2022: Global energy spectrum of the general oceanic circulation. *Nat. Commun.*, **13**, 5314, <https://doi.org/10.1038/s41467-022-33031-3>.
- Sugimoto, N., and R. Plougonven, 2016: Generation and backreaction of spontaneously emitted inertia-gravity waves. *Geophys. Res. Lett.*, **43**, 3519–3525, <https://doi.org/10.1002/2016GL068219>.
- Torres, H. S., P. Klein, D. Menemenlis, B. Qiu, Z. Su, J. Wang, S. Chen, and L.-L. Fu, 2018: Partitioning ocean motions into balanced motions and internal gravity waves: A modeling study in anticipation of future space missions. *J. Geophys. Res. Oceans*, **123**, 8084–8105, <https://doi.org/10.1029/2018JC014438>.
- , and Coauthors, 2019: Diagnosing ocean-wave-turbulence interactions from space. *Geophys. Res. Lett.*, **46**, 8933–8942, <https://doi.org/10.1029/2019GL083675>.
- Vallis, G., 2006: *Atmospheric and Ocean Fluid Dynamics: Fundamentals and Large-Scale Circulation*. 2nd ed. Cambridge University Press, 745 pp.
- Zhao, Z., 2020: Southward internal tides in the northeastern South China Sea. *J. Geophys. Res. Oceans*, **125**, e2020JC016554, <https://doi.org/10.1029/2020JC016554>.
- , 2021: Seasonal mode-1 M_2 internal tides from satellite altimetry. *J. Phys. Oceanogr.*, **51**, 3015–3035, <https://doi.org/10.1175/JPO-D-21-0001.1>.
- , J. Wang, D. Menemenlis, L.-L. Fu, S. Chen, and B. Qiu, 2019: Decomposition of the multimodal multidirectional M_2 internal tide field. *J. Atmos. Oceanic Technol.*, **36**, 1157–1173, <https://doi.org/10.1175/JTECH-D-19-0022.1>.